

Towards Patient-Individual Blood Flow Simulations based on PC-MRI Measurements

Sebastian Meier^{*†} Anja Hennemuth[†] Nikola Tchipev[†] Andreas Harloff[‡]
Michael Markl[§] Tobias Preusser[¶]

Abstract: Computational haemodynamics based on CT or MRI tomographic scans of individual patient vessel anatomy can be a valuable tool for therapy decision in cardiovascular and cerebrovascular diseases. Current approaches are promising, but still suffer from complex model generation, poor knowledge of haemodynamical parameters and high computational costs. We present a new approach of constructing patient-individual flow models that is based on additional knowledge from 4D PC-MRI data, and on the Lattice-Boltzmann method as an alternative flow solver. It potentially allows for easier assembling of models, improved accuracy and faster computations by massive parallelization. In this paper, we verify our method for a stenotic flow phantom by comparison with an established CFD solver, and we test the method in order to simulate systolic flow in a carotid bifurcation and compare it to the 4D PC-MRI flow data.

1 Introduction

Quantification of intravascular blood flow properties (haemodynamics) is of high importance in clinical practice for diagnosis of cardiovascular and cerebrovascular disorders and intervention planning. Important examples are the assessment of stroke risk in patients with carotid or intracranial stenosis and cerebral aneurysma and the diagnosis of age-related or congenital heart defects. Improved diagnosis and prediction of flow properties can help understanding mechanisms of stenosis development and progression and give support in endovascular treatment planning. In current clinical practice, the most important cardiological tools for quantification of blood flow are external blood pressure measurement by the Riva-Rocci method, Doppler ultrasound and invasive catheter measurements. On radiological side, widely used imaging modalities are contrast-enhanced MRI and CT angiography (MRA, CTA), digital subtraction angiography and two-dimensional phase-contrast MRI (2D PC-MRI). The latter modality has the benefit of being non-invasive, radiation- and contrast-free and yields time-resolved 2D velocity profiles over the cross

*sebastian.meier@mevis.fraunhofer.de

†Fraunhofer MEVIS, Bremen, Germany

‡Department of Neurology, University Hospital Freiburg, Germany

§Departments of Radiology and Biomedical Engineering, Northwestern University Feinberg School of Medicine

¶School of Engineering and Science, Jacobs University, Bremen, Germany

section of a vessel. In the past decade, it has been further developed to a fully time- and spatially resolved imaging method (4D PC-MRI) [SLWL09, HHP⁺10]. In addition to clinically established local diagnostic parameters like mean flow rate or peak velocities, 4D PC-MRI offers the assessment of complex flow patterns and particle trajectories in three-dimensional regions of interest and the computation of pressure difference maps [MHF⁺10]. Its application in various medical fields is currently an active research field and will achieve its broad clinical use in the next years.

1.1 Image-based computational haemodynamics

The advances in MRI and CT imaging as well as increased computational possibilities have inspired also mechanical and mathematical research groups to apply methods of Computational Fluid Dynamics (CFD) in order to simulate blood flow in individual patient geometries. CFD methods are nowadays well established in industrial product design, and several mature and flexible commercial software packages exist for performing accurate CFD studies, provided that the exact three-dimensional geometry is known. In current research projects, CFD methods are tested, e.g., for determining the rupture risk of cerebral aneurysms [CSP10, SJR⁺09], the effectiveness of plugged stents [AML⁺09] or for investigating the influence of wall shear stress on arteriosclerosis development [HNB⁺10]. The vessel anatomy is typically obtained from CTA or MRA images of the vessels.

Although results are promising and accurate prediction of patient-individual blood flow has already proved feasible in certain cases, the clinical use of CFD methods is still hampered by several problems:

1. The computational effort is still large even for simplest possible flow models. In many cases, a large amount of the computation time is spent for the complex mesh generation. More complex model properties like pulsatile flow, non-Newtonian flow models and fluid-structure interaction drastically increase the computational costs.
2. The simulation results depend strongly on the choice of inflow and outflow conditions. These conditions involve the fixation or extrapolation of unknown velocities or pressure values, and are in reality often not met.
3. Important vessel parameters like elasticity and wall thickness are patient-dependent and not known exactly, and, therefore, wall motion is difficult to account for.
4. The workflow for constructing the models is complex and user-dependent, and currently it can only be done by CFD experts. Except from very few research tools, no specialized software tools exist for performing computational haemodynamics.

In recent studies it has been indicated that the problem of setting realistic inlet- and outlet conditions (problem no. 2) can be successfully tackled with a combination of in-vivo PC-MRI measurements and CFD computations [CPA⁺09, GJS⁺11, RBAB⁺08, KYG⁺09]. However, the flow geometry in these works is still obtained from additional CTA or MRA

scans, while the full three-dimensional flow information from 4D PC-MRI data is not yet efficiently used in the model generation.

1.2 Lattice-Boltzmann blood flow simulations

Most blood flow simulation approaches are based on classical numerical solvers of incompressible Newtonian flow like the finite-volume method or finite-element method, e.g. [APB⁺08, TF09, CPA⁺09]. Recently, the Lattice-Boltzmann method has been suggested and further developed as an alternative blood flow solver [AHS06, HDV09, SGR⁺09, BHS⁺06].

Since about 1990, the Lattice-Boltzmann method (LBM) has gained popularity as an alternative numerical method for simulating flow on a mesoscopic scale. It simulates the dynamics of particle distributions based on the Boltzmann equation from statistical physics [Suc01, WG00, CD98]. After appropriate rescaling of variables, it is naturally defined on a cubic lattice in d -dimensional space with unit grid spacing together with a set of discrete lattice direction vectors $\{\mathbf{e}_\alpha\}_{\alpha=0,\dots,q-1}$ defining a local neighborhood of a grid point. In the D3Q19 model, the neighborhood consists of the 18 neighboring grid points with distance smaller or equal to $\sqrt{2}$, whereas in the D3Q27 model the neighborhood contains a full cube of side length 2. In one time step, particles can move along the lattice only in the given lattice directions. Consequently, at each grid point \mathbf{x} and time t , one defines one distribution function $f_\alpha(\mathbf{x}, t)$ of particles moving in each of the q directions. The LBM iteration with Bhatnagar–Gross–Krook (BGK) approximation for the collision term reads

$$f_\alpha(\mathbf{x} + \mathbf{e}_\alpha, t + 1) - f_\alpha(\mathbf{x}, t) = -\frac{1}{3\nu + 1/2} \left(f_\alpha(\mathbf{x}, t) - f_\alpha^{(\text{eq})}(\rho, \mathbf{u}) \right), \quad \alpha = 0, \dots, q-1,$$

where ν is the lattice viscosity, and the equilibrium distributions $f_\alpha^{(\text{eq})}(\rho, \mathbf{u})$ for given fluid density ρ and velocity \mathbf{u} are defined as

$$f_\alpha^{(\text{eq})}(\rho, \mathbf{u}) = \rho t_\alpha \left(1 + 3\mathbf{e}_\alpha \cdot \mathbf{u} + \frac{9}{2} |\mathbf{e}_\alpha \cdot \mathbf{u}|^2 - \frac{3}{2} |\mathbf{u}|^2 \right).$$

The weights t_α are lattice-dependent constants and can be found in the literature, e.g. [QDL92, WG00]. The macroscopic flow quantities are computed from the particle distributions via

$$\rho = \sum_{\alpha=0}^{q-1} f_\alpha, \quad \rho \mathbf{u} = \sum_{\alpha=0}^{q-1} \mathbf{e}_\alpha f_\alpha, \quad p = \frac{1}{3}(\rho - 1).$$

Since flow pressure p is directly related to the density, the LBM scheme is actually a compressible scheme. However, for appropriate choice of scaling, the density variations are small and it is proven to be an effective approximation to the incompressible Navier-Stokes equations [WG00].

The main advantages of the Lattice-Boltzmann method compared to the classical solvers are:

- It is defined naturally on a cubic grid and can be easily assembled also in complex-shaped geometries.
- It has a simple, iterative algorithm that is straight-forwardly parallelizable.
- Its explicit time-discretisation makes it well-suited for modeling time-dependent, pulsatile flow.
- Physical quantities like shear-stress and pressure can be directly computed from the local particle distributions without further post-processing steps.

1.3 Purpose of this work

In this work, we introduce a new workflow for construction and evaluation of patient-specific blood flow simulation models based on PC-MRI measurements and the LBM numerical method. The goal of such a combination is to relax the main limitations of both methods, namely the limited resolution and image quality of 4D PC-MRI and the lack of information in the construction of CFD models. We believe that, due to its explicit and parallel nature, the LBM scheme has the potential to be an efficient method for detailed flow analysis and future testing of surgical or endovascular therapy options.

Our software workflow involves state-of-the art image processing algorithms, massive-parallel computations and efficient data processing. This is particularly relevant for large PC-MRI data sets and the typically large CFD models of several millions of grid nodes.

In the methods section, we summarize the basic steps of PC-MRI data processing and CFD model generation. All image processing steps are implemented in MeVisLab, while the LBM computations are done with the open-source library Palabos [LM11]. The methods are first applied to a stenotic vessel phantom, where, on top of the measurements, a numerical solution from a commercial flow solver is available for verification of our method. Afterwards, in-vivo PC-MRI measurements of a carotid artery bifurcation are used to construct a CFD model. The results are presented and compared to the measured data in the results section.

2 Methods

2.1 PC-MRI image acquisition

The flow phantom consisted of a rigid pipe with diameter $d_{in} = 33.5\text{mm}$ containing a 90%-stenosis of diameter $d_s = 10.3\text{mm}$, connected to a stationary flow pump with a flow rate of approximately 0.2 l/s (see also figure 1). As a blood-mimicking fluid, a water-ethanol mixture was used with density and viscosity comparable to blood. PC-MRI flow measurements were performed with a Siemens 3T scanner with a velocity encoding (VENC) of 1.5m/s and an isotropic voxel size of 1mm. Measured maximum velocity was

$u_{in} = 0.2\text{m/s}$ before the stenosis and $u_s = 1.3\text{m/s}$ inside the stenosis. Assuming a kinematic blood viscosity of $\nu = 4\text{mm}^2/\text{s}$, the corresponding Reynolds numbers $\text{Re} = \frac{du}{\nu}$ are 1675 and 3348, respectively.

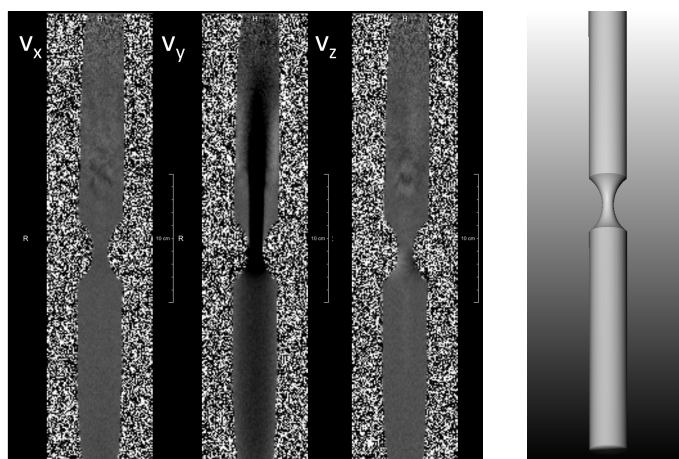


Figure 1: PC-MRI data of flow phantom with 90% stenosis (left) and constructed surface model (right).

In-vivo carotid artery measurements were obtained from a healthy 25-year old volunteer with a large bulb at the internal carotid artery (ICA) using the same scanner (figure 3). Data was acquired in an axial 3D slab covering both the left and right carotid bifurcation ($V_{ENC} = 1\text{m/s}$). The voxel size was 0.86mm in x - and y -direction and 1.4mm in z -direction, and the temporal resolution was 0.045s . Systolic velocity at the left common carotid artery (CCA) was $u_{in} = 0.7\text{m/s}$ at a diameter of 7mm , which corresponds to a Reynolds number of 1225.

2.2 PC-MRI data correction steps

PC-MRI data consist of four 4D data sets showing the flow magnitude and the velocity components for the three spatial encoding directions. Typical errors in these data, which hamper the flow analysis, are eddy currents and phase wraps.

Eddy Current Correction Eddy currents in the electromagnetic field are assumed to introduce spatially and temporally slowly varying image gradients, which are added to the phase images that encode the flow velocities in the three dimensions. As proposed by Lankhaar et al. the correction of this effect is performed by fitting polynomial planes to the velocities of static non-moving regions [LHM⁺05]. This static tissue mask ST is determined by thresholding the velocity standard deviation over time. Figure 2 shows an example for the eddy current error images computed for an aorta data set.

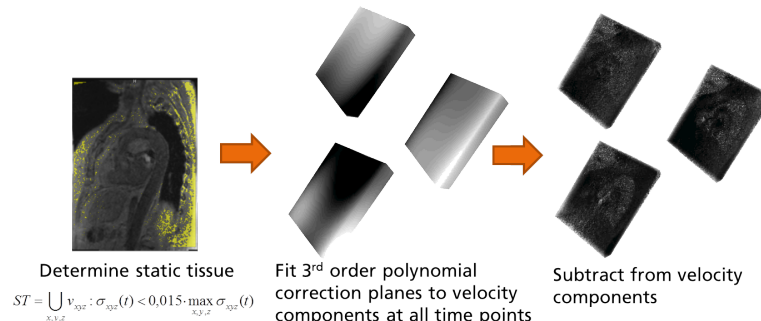


Figure 2: Eddy current correction using a static tissue mask.

Phase Unwrapping Measured phase (velocity) values are usually mapped to integer values between 0 and 4095. The value range encoded in this interval is determined by the VENC, which is adjusted through the gradient strength and duration. If the actual blood flow velocity u during the image acquisition exceeds the velocity encoding, so called phase wraps occur and the measured velocity u_{VENC} is

$$u_{VENC} = -\frac{u}{|u|} (\text{VENC} - |u| \bmod \text{VENC}) . \quad (1)$$

Phase wraps are detected and corrected by applying the reliability measure proposed by Diaz et al. in an iterative process [DR04].

2.3 Generation of a vessel surface model

The shape of the stenotic flow phantom was measured by hand and a corresponding software phantom was constructed and meshed in MATLAB. The total length of the software phantom (1000mm) is longer than the actual flow phantom length to be able to fully simulate the long flow jets arising from the narrow stenosis (see figure 1).

For the in-vivo measured data sets, the surface mesh is constructed from image data by the following steps (figure 3): First, a semi-automatic watershed segmentation is done on the PC-MRA image, which contains an average over all time steps of the magnitude image, enhanced by the flow information from the three phase images [HFS⁺11]. The resulting mask image is skeletonized and represented as a graph structure, where each vessel skeleton contains information of its distance to the vessel wall (*step a*) [BHH⁺05]. The subtree of the vessel system relevant for the simulation model is interactively extracted. For our example of the carotid artery this means in particular that the smaller vessels leaving the external carotid artery (ECA) have been ignored for the flow model. All inlets and outlets are then artificially extended by a pipe segment of suitable size (*step b*). These so-called *flow extensions* are a standard approach in CFD needed in order to avoid instabilities and errors due to a non-fully developed laminar pipe flow profile at the inlets and outlets. In

our example case, a minimum of 15mm at the outlets and a minimum of 5mm at the inlets is chosen. From the resulting graph structure, a triangular surface mesh is constructed, which is smooth at the junctions and endings.

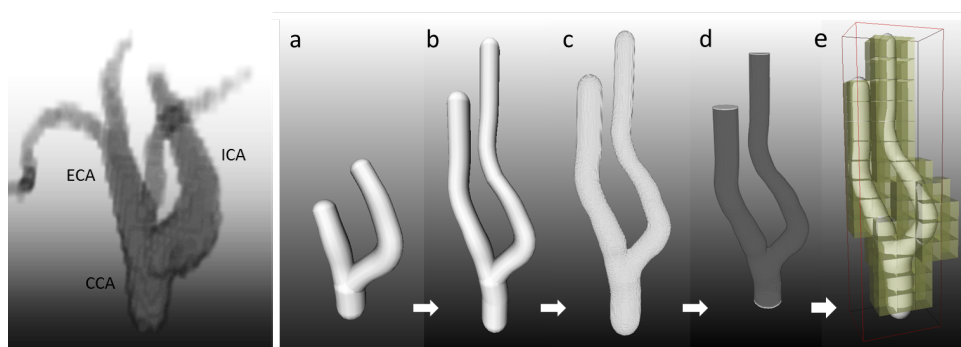


Figure 3: Original segmentation mask (left) and different steps in the construction of the CFD geometry (right).

2.4 Multi-block lattice generation

The surface model is voxelized to the required grid resolution. In the LBM method, a sufficiently fine resolution is not only required for accuracy, but also for stability in case of high flow velocities. For the carotid bifurcation, an isotropic resolution of 0.07mm is chosen, while for the flow phantom with lower flow velocities a resolution of 0.69mm was chosen (see also table 1).

The resulting voxelized image is a binary mask of the vessel system in the required resolution for the LBM solver. In this image, 2D rectangular boxes are defined along the directions of the image coordinate system for setting the inlet and outlet conditions and the mask is modified correspondingly (*step d*). Finally, an octree decomposition of the mask image into cubes of uniform side length of power 2 is performed up to a certain level $\ell_d \geq 1$, in order to save memory and to be able to distribute the resulting blocks to the different threads for MPI-parallel flow computations (*step e*). The optimal value of ℓ_d depends on the size and shape of the vessel system, on the memory available and on the degree of desired parallelization (see table 1 for an overview). The LBM grid of the carotid artery data set has a bounding box of $219 \times 278 \times 986$ voxels, but contains only 11% fluid voxels. Memory allocation of the whole rectangular block for the D3Q19 model in double precision would require 9GB of memory. An octree decomposition of the surrounding cubic block of side length 1024 up to level 4 results in 4069 subblocks of size length 64, but only 111 contain fluid nodes and need to be allocated, which results in memory allocation of only 4.9GB.

2.5 Distributed-memory parallel flow simulation

The stationary LBM computations are performed with the open-source Lattice-Boltzmann library Palabos [LM11]. For density and kinematic viscosity of blood, the constant values $\rho = 1060\text{kg/m}^3$ and $\nu = 4\text{mm}^2/\text{s}$ are chosen, which is a good approximation for blood vessels considerably larger than a few micrometers. All physical quantities are scaled to the lattice coordinate system and the lattice is constructed from the binary mask such that each voxel center position corresponds to one lattice node. Fluid nodes are initialized with standard BGK dynamics, while non-fluid nodes within the atomic blocks are allocated but initialized with full-way Bounce-Back dynamics, such that almost no computations are required in these nodes. The atomic blocks are equally distributed to the available threads, where every block is surrounded by one extra layer of lattice nodes for performing the streaming step in each iteration.

Regularized boundary conditions are chosen for the open boundaries [Lat07]. On the inlets, a fully developed laminar Poiseuille profile is given as Dirichlet conditions, which correspond to the systolic time-peak spatial-mean flow rates measured from the PC-MRI velocity data. On the outlets, tangential components of the velocity are set to zero while the pressure value is set to a suitable value (typically zero). Zero velocity and pressure values are set as initial conditions. In order to avoid the rise of unphysical pressure waves, all Dirichlet conditions are smoothly adjusted from zero to their target values during the first iterations.

In order to check for convergence of the iterative solution procedure, results of subsequent iterations need to be compared and traced. Since a comparison of particle distributions in the whole flow domain is too expensive and memory-consuming, relevant subdomains are defined, at which velocity and pressure are traced every 200 iterations. When the relative RMS norm of the difference of subsequent traced quantities on all these subdomains becomes smaller than a given tolerance, convergence is indicated. Reasonable tolerance levels depend on resolution and on the expected turbulence level. Typical values in our examples are 10^{-3} for velocity and 10^{-4} for pressure convergence.

2.6 Result processing and visualization

For post-processing, each thread writes out subsampled images of its computed velocity and pressure data in parallel. Subsampling becomes important with large grid sizes for speedup in post-processing and visualization of the results, for which the high lattice resolution is often not needed. The data blocks are composed back to 3D images and are further processed and visualized page-based in MeVisLab. This pipeline has been proven efficient even for very large computational grids. Advanced post-processing like multi-planar resolution views (MPRs) and particle tracing are done with a research software specialized for 4D PC-MRI data [HFS⁺11].

3 Results

In total, the results of three simulations are presented. The discretisation details are summarized in table 1.

case	u_{in} (m/s)	resol. (mm)	bounding box	ℓ_d	block size	# blocks	# nodes fluid, alloc.	Mem. (GB)
phantom	0.04	0.69	$53 \times 53 \times 1460$	5	64	23	$2.7 \cdot 10^6$ $6.0 \cdot 10^6$	1.0
phantom	0.2	0.52	$86 \times 84 \times 586$	-	147	4	$2.2 \cdot 10^6$ $4.2 \cdot 10^6$	0.6
in-vivo	1.0	0.07	$219 \times 278 \times 986$	4	64	111	$6.8 \cdot 10^6$ $31.9 \cdot 10^6$	4.9

Table 1: Sizes and decomposition details of the simulation models. The second case was not decomposed with the octree algorithm but manually.

3.1 Stenotic flow phantom

In order to verify our LBM simulation results, a reference CFD solution for the flow phantom was computed using the commercial Finite-Element toolbox COMSOL Multiphysics. A rotationally symmetric 2D model of the flow phantom was constructed and meshed with a grid size of 0.5mm, where grid independence was assured. In order to be in a laminar flow regime, the inlet velocity for this comparison was reduced to $u_{in} = 0.02\text{m/s}$. The reference solution is plotted in figure 4. For the same inlet velocity, a flow model was constructed and solved with the LBM method as described in the previous section. Since the D3Q19 model produced unphysical anisotropies in the flow jet after the stenosis at the chosen resolution (cf. also [WC11]), the more accurate D3Q27 model was chosen for this simulation. Both results are compared (figure 5). The axial pressure and the radial velocity profiles at the stenosis are in very good agreement, whereas the radial profiles after the stenosis ($z = 500\text{mm}$) are affected by a radial shift of the flow jet.

The original flow model with inlet velocity equal to that of the PC-MRI data set ($u_{in} = 0.2\text{m/s}$) shows strong turbulent behavior, due to the high-velocity flow jet arising after the stenosis. The turbulences are not visible in the PCMRI measurements due to signal loss, but can be clearly seen in the results of a preliminary simulation with artificially increased viscosity ($\nu = 15\text{mm}^2/\text{s}$), which reduces turbulences (figure 6). The overall structure of the flow jet can be recovered already in this simulation, but the turbulent behavior starts at a later axial position than in the measurement.

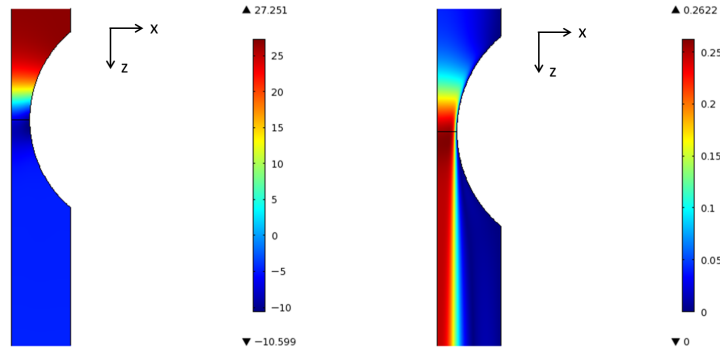


Figure 4: Reference solution for flow phantom at low velocity: pressure (left) and velocity magnitude (right).

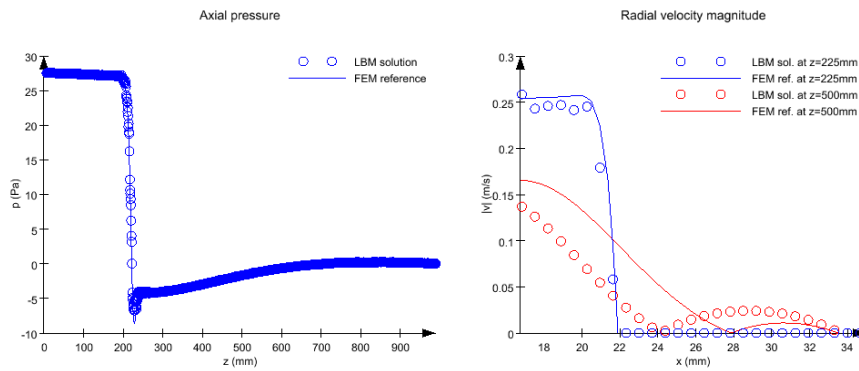


Figure 5: Axial pressure (left) and radial velocity magnitude profiles (right) computed with LBM compared to the reference solution at two different axial positions.

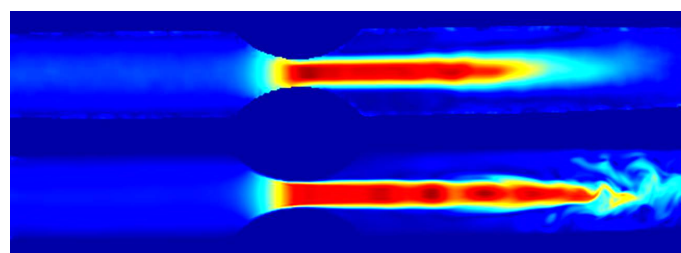


Figure 6: Velocity magnitude in flow phantom at high velocity: original PC-MRI data (top) and flow simulation with artificially increased blood viscosity (bottom).

3.2 In-vivo data set

A CFD model was constructed for the volunteer data set and a stationary LBM simulation was done on the basis of the peak-systolic spatial-mean flow rates in the PC-MRI mea-

surements and compared with the corresponding systolic PC-MRI velocity field. In figure 7, velocity profiles at three positions are compared with the measurements. The MPR images are obtained by interpolating the velocity data to the oblique slices representing the vessel cross section. Since the simulation results are given with higher resolution, also the corresponding MPRs are higher resolved.

In figure 8, flow pathlines are shown for both cases. The surface model in both figures corresponds to the simulation domain. While the primary flow behavior and the velocity magnitudes agree well, the measurements show some secondary flow patterns within the ICA bulb, which is not seen in the simulation. A comparison with the aforementioned Finite-Element solver was not feasible for this case, due to its limitations in treating complex geometries.

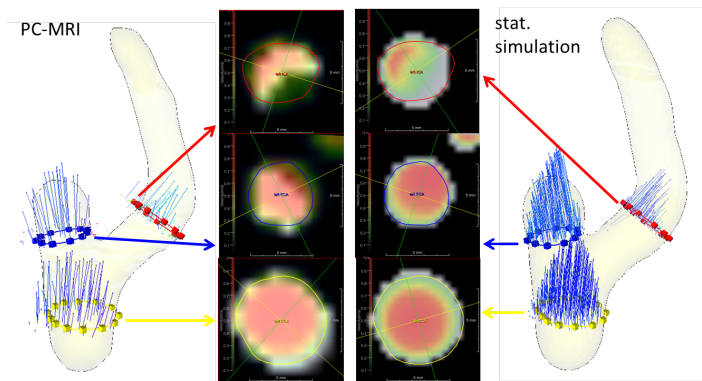


Figure 7: Comparison of systolic velocity profiles in left carotid artery.

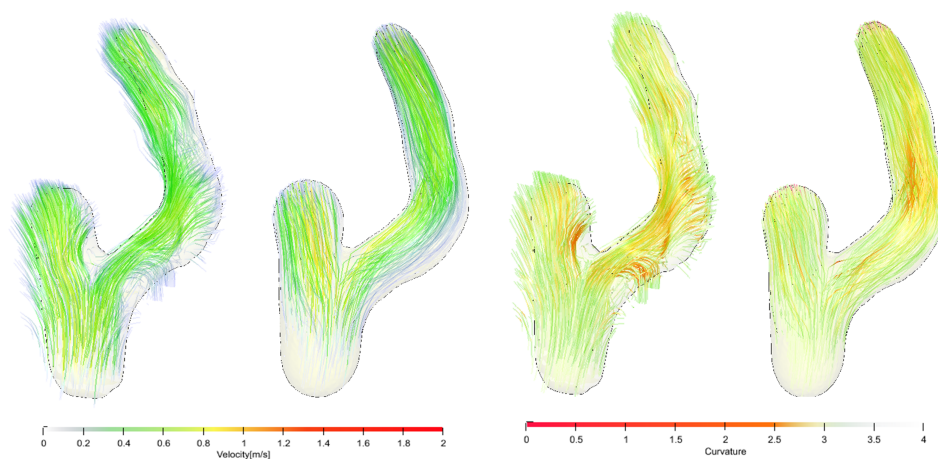


Figure 8: Comparison of systolic flow pathlines in left carotid artery with color encoding by velocity (left) and curvature (right). Left pathlines are computed from measurements, right pathlines from simulation results.

4 Discussion

The overall workflow described above consists of PC-MRI image acquisition and advanced processing, generation of the CFD model, flow computation and finally post-processing and extraction of desired result data. In the presented in-vivo example, only contrast- and radiation-free PC-MRI measurements of a healthy carotid bifurcation have been used for obtaining vessel anatomy and flow information. This differs from most other CFD approaches, in which higher-resolved CTA or MRA images are used for anatomy extraction. It needs to be clarified in further studies, for which applications the latter type of image acquisition is really necessary. Moreover, the quantitative 4D velocity information has been used in the presented examples only for setting the inlet velocity. For improved model accuracy, this information could be used more extensively in the model generation.

The other important difference compared to other CFD approaches is that our methodology goes completely without complex mesh generation. This makes it particularly useful for complex vessel systems, and, perspective, also for modeling non-rigid moving vessels like the aorta or heart ventricles. However, in the presented example, the simulated vessel system was highly simplified and the performance for more complex systems still needs to be tested.

A first evaluation of the accuracy of the flow solver was done for a phantom model of a stenotic vessel. At low flow velocities, simulated velocity and pressure profiles are in good agreement with the CFD reference solution, except of the precise radial position of the flow jet after stenosis. Flow jets at high Reynolds numbers are known to behave unstable, so this effect is probably caused by low grid resolution and the stair-case approximation of the vessel wall at the stenosis. It needs to be further investigated by doing a proper convergence study. The error is expected to be highly reduced by adding a smooth vessel wall treatment to the LBM model (cf. [AHS06, HDV09]). The high-velocity turbulent simulation is currently not feasible with our available computer hardware, but a simulation with reduced Reynolds number already shows quite realistic behavior. In particular, the simulation shows fine-scale details of the vortices after stenosis that are completely smeared out in the PC-MRI measurements. Depending on the desired degree of details in the simulation, turbulence models might be used in future to get accurate average quantities out of such a flow model. However, it should be mentioned that most flow scenarios in non-pathological human vessels are *not* turbulent, so this 90% stenosis example case can be regarded already as a “worst-case situation” for a numerical model.

The general flow behavior for the CFD model from the volunteer data set is comparable to the PC-MRI data. However, the differences are larger than for the phantom data sets. There are two main reasons for this: First, effects due to pulsatile flow are not covered by the stationary simulation. And second, the constructed surface model shows considerable differences at the ICA trunk due to the approximations of the graph representation, in particular the assumption of circular vessel cross sections. Both facts need to be accounted for in further development of the methodology and to be evaluated in larger patient studies.

Finally we discuss the feasibility of the overall workflow as an integrated software tool for clinical decision-making. In all mentioned steps, large data sets of several hundreds

of megabytes need to be processed, which makes dedicated algorithms necessary. The page-based pre- and post-processing in MeVisLab appears to be well suitable for these tasks. The efficient data exchange with the parallel threads of the flow solver also avoids long loading and saving times compared to other workflows with distinct pre-processing, solving and post-processing software. However, the performance and usability can still be highly improved and will be quantified in further studies.

5 Conclusions

It has been shown in a couple of first examples that the proposed workflow for constructing of reliable CFD models from PC-MRI data sets is feasible. By efficient data processing and parallelization, it is potentially applicable also for more complex vessel systems and even larger data sets. By reducing the manual interaction steps involved, the methodology may become a clinically usable tool for advanced flow diagnosis and treatment planning.

The evaluation of the simulation results and comparison to the data partly shows good agreement. The full potential of the LBM-based flow simulations cannot be accessed yet, due to some simplifications made mainly for technical reasons. These restrictions are the graph-based surface representation, the stationary simulations and the ad-hoc setting of pressure levels and will be accounted for in future work. Further studies with advanced methodology will be done on larger patient and volunteer groups and include also comparison with preprocessing methods from higher resolved CTA or MRA images.

Acknowledgments

This work was partly funded by the European Regional Development Fund (EFRE).

References

- [AHS06] A. M. Artoli, A. G. Hoekstra, and P. M. A. Sloot. Mesoscopic simulations of systolic flow in the human abdominal aorta. *J Biomech*, 39(5):873–884, 2006.
- [AML⁺09] S. Appanaboyina, F. Mut, R. Löhner, C. Putman, and J. Cebal. Simulation of intracranial aneurysm stenting: Techniques and challenges. *Computer Methods in Applied Mechanics and Engineering*, 198(45–46):3567–3582, 2009.
- [APB⁺08] L. Antiga, M. Piccinelli, L. Botti, B. Ene-Iordache, A. Remuzzi, and D. A. Steinman. An image-based modeling framework for patient-specific computational hemodynamics. *Med Biol Eng Comput*, 46(11):1097–1112, 2008.
- [BHH⁺05] T. Boskamp, H. K. Hahn, M. Hindennach, S. Oeltze, B. Preim, S. Zidowitz, and H. O. Peitgen. *Medical Imaging Systems*, chapter Geometrical and Structural Analysis of Vessel Systems in 3D Medical Image Datasets, pages 1–60. World Scientific, 2005.

- [BHS⁺06] J. Bernsdorf, S. E Harrison, S. M Smith, P. V. Lawford, and D. R. Hose. Concurrent numerical simulation of flow and blood clotting using the lattice Boltzmann technique. *Int J Bioinform Res Appl*, 2(4):371–380, 2006.
- [CD98] S. Chen and G. D. Doolen. Lattice Boltzmann Method for Fluid Flow. *Annu. Rev. Fluid Mech.*, 30:329–364, 1998.
- [CPA⁺09] J. R. Cebal, C. M. Putman, M. T. Alley, T. Hope, R. Bammer, and F. Calamante. Hemodynamics in Normal Cerebral Arteries: Qualitative Comparison of 4D Phase-Contrast Magnetic Resonance and Image-Based Computational Fluid Dynamics. *J Eng Math*, 64(4):367–378, 2009.
- [CSP10] J. R. Cebal, M. Sheridan, and C. M. Putman. Hemodynamics and bleb formation in intracranial aneurysms. *AJNR Am J Neuroradiol*, 31(2):304–310, 2010.
- [DR04] C. Diaz and L. A. Robles. Fast Noncontinuous Path Phase-Unwrapping Algorithm Based on Gradients and Mask. In A. Sanfeliu, M. Trinidad, J. Francisco, C. Ochoa, and J. Ariel, editors, *Progress in Pattern Recognition, Image Analysis and Applications*, volume 3287 of *Lecture Notes in Computer Science*, pages 116–123. Springer Berlin / Heidelberg, 2004.
- [GJS⁺11] R. Gasteiger, G. Janiga, D. Stucht, A. Hennemuth, O. Friman, O. Speck, M. Markl, and B. Preim. Vergleich zwischen 7 Tesla 4D PC-MRI Flussmessung und CFD-Simulation. In *Bildverarbeitung für die Medizin (BVM)*, pages 304–308, Lübeck, 2011.
- [HDV09] X. He, G. Duckwiler, and D. J. Valentino. Lattice Boltzmann simulation of cerebral artery hemodynamics. *Computers & Fluids*, 38(4):789–796, 2009.
- [HFS⁺11] A. Hennemuth, O. Friman, C. Schumann, J. Bock, J. Drexl, M. Huellebrand, M. Markl, and H.-O. Peitgen. Fast interactive exploration of 4D MRI flow data. In K. H. Wong and D. R. Holmes, editors, *Medical Imaging 2011: Visualization, Image-Guided Procedures, and Modeling*, volume 7964, page 79640E. SPIE, 2011.
- [HHP⁺10] T. A Hope, M. D Hope, D. D. Purcell, C. von Morze, D. B. Vigneron, M. T. Alley, and W. P. Dillon. Evaluation of intracranial stenoses and aneurysms with accelerated 4D flow. *Magn Reson Imaging*, 28(1):41–46, 2010.
- [HNB⁺10] A. Harloff, A. Nussbaumer, S. Bauer, A. F. Stalder, A. Frydrychowicz, C. Weiller, J. Hennig, and M. Markl. In vivo assessment of wall shear stress in the atherosclerotic aorta using flow-sensitive 4D MRI. *Magn Reson Med*, 63(6):1529–1536, 2010.
- [KYG⁺09] C. Karmonik, C. Yen, R. G. Grossman, R. Klucznik, and G. Benndorf. Intra-aneurysmal flow patterns and wall shear stresses calculated with computational flow dynamics in an anterior communicating artery aneurysm depend on knowledge of patient-specific inflow rates. *Acta Neurochir (Wien)*, 151(5):479–85, 2009.
- [Lat07] J. Latt. *Hydrodynamic limit of lattice Boltzmann equations*. PhD thesis, Univ. Genève, 2007.
- [LHM⁺05] J. Lankhaar, M. B. M. Hofman, J. T. Marcus, J. J. M. Zwanenburg, T. J. C. Faes, and A. Vonk-Noordegraaf. Correction of phase offset errors in main pulmonary artery flow quantification. *J Magn Reson Imaging*, 22(1):73–79, 2005.
- [LM11] J. Latt and O. Malaspinas. Palabos – Parallel Lattice Boltzmann Solver. Web page, June 2011. www.lbmethod.org/palabos.

- [MHF⁺10] S. Meier, A. Hennemuth, O. Friman, M. Markl, and T. Preusser. Noninvasive 4D Blood Flow and Pressure Quantification in Central Blood Vessels via PCMRI. *Online Archives of Computing in Cardiology*, 37, 2010.
- [QDL92] Y. H. Qian, D. D’Humières, and P. Lallemand. Lattice BGK Models for Navier-Stokes Equation. *EPL (Europhysics Letters)*, 17(6):479, 1992.
- [RBAB⁺08] V. L. Rayz, L. Boussel, G. Acevedo-Bolton, A. J. Martin, W. L. Young, M. T. Lawton, R. Higashida, and D. Saloner. Numerical simulations of flow in cerebral aneurysms: comparison of CFD results and in vivo MRI measurements. *J Biomech Eng*, 130(5):051011, 2008.
- [SGR⁺09] M. Stürmer, J. Götz, G. Richter, A. Dörfler, and U. Rude. Fluid flow simulation on the Cell Broadband Engine using the lattice Boltzmann method. *Computers & Mathematics with Applications*, 58(5):1062 – 1070, 2009.
- [SJR⁺09] S. Seshadhri, G. Janiga, G. Rose, B. Preim, M. Skalej, and D. Thévenin. Investigations of steady and unsteady flows in an aortic aneurysm. In *1st International Conference on Mathematical and Computational Biomedical Engineering CMBE, Swansea, UK*, pages 246–249. Nithiarasu, P., Löhner, R., and van Loon, R., 2009.
- [SLWL09] M. B. Srichai, R. P. Lim, S. Wong, and V. S. Lee. Cardiovascular applications of phase-contrast MRI. *AJR Am J Roentgenol*, 192(3):662–675, 2009.
- [Suc01] S. Succi. *The Lattice Boltzmann Equation for Fluid Dynamics and Beyond*. Oxford University Press, 2001.
- [TF09] C. A. Taylor and C. A. Figueroa. Patient-specific modeling of cardiovascular mechanics. *Annu Rev Biomed Eng*, 11:109–134, 2009.
- [WC11] A. T. White and C. K. Chong. Rotational invariance in the three-dimensional lattice Boltzmann method is dependent on the choice of lattice. *Journal of Computational Physics*, 230(16):6367–6378, 2011.
- [WG00] D. A. Wolf-Gladrow. *Lattice-Gas Cellular Automata and Lattice Boltzmann Models: An Introduction*. Springer, 2000.